Development of a Method for Thermogalvanic Characterization of Li-Ion Electrodes: A Case Study in Thin-Film Anatase TiO$_2$

Liese B. Hubrechtsen[ab] and Philippe M. Vereecken[ab]*

[a]KU Leuven Centre for Membrane Separations, Adsorption, Catalysis, and Spectroscopy for Sustainable Solutions, Celestijnenlaan 200f - box 2454, Leuven, 3001, Belgium

[b]imec, Kapeldreef 75, Leuven, 3001, Belgium

ABSTRACT

The Internet-of-Things will require innovative solutions to power wireless or remote sensor nodes, for instance via harvesting heat from the environment to produce electricity. Thermogalvanic and Thermally Regenerative Electrochemical Cycle (TREC) cells are an interesting approach for such systems due to their high temperature responses. Both of these strategies rely on the temperature dependence of an electrochemical equilibrium potential, i.e. the thermogalvanic effect. However, whereas thermogalvanic cells operate under a fixed temperature gradient, TREC harvesting is instead accomplished by charging and discharging an electrochemical cell at different

temperatures. The use of thin-film Li-ion batteries in these devices can enable great advantages in terms of performance and scalability. However, existing approaches to determine thermogalvanic coefficients in Li-ion materials are not suitable as screening techniques that can provide reliable coefficient values for device design. This work presents a novel methodology to characterize thermogalvanic profiles, i.e. the dependence of the thermogalvanic coefficient on the lithiation state, for Li-ion electrodes. To this end, a thermogalvanic cell featuring thin-film electrodes and an electrochemically-controllable lithiation state was used and operated with an iterative procedure. When preventing charge difference accumulation via compositional levelling, the presented method enabled precise and high-resolution measurements of the thermogalvanic profile. Validation of the methodology was performed by measuring the profile of thin-film anatase TiO_2, a commonly studied Li-ion electrode material, and demonstrating it to be in excellent agreement with accepted phase behavior. Moreover, the identification of nanoscaling effects in this profile highlighted the strength of this approach. This work may open the door to further research in the field of thermogalvanic harvesting using Li-ion materials for the Internet-of-Things.

1. Introduction

During the coming years, the Internet-of-Things (IoT) is expected to gain increasing importance both in industrial settings and everyday lives (1). Ideally, the sensing nodes that form the backbone of this technology will ultimately be downscaled and made wireless, taking the form of "smart dust" (2). It is crucially important to identify a way to power these components: as some nodes may be placed in inaccessible or even dangerous locations, self-sufficient systems that can harvest

energy from their environments are desired. Low-grade heat ($< 250°C$) is an especially interesting source for such harvesting strategies, as it is ubiquitously available.

The most well-established strategy for heat-to-electricity harvesting is based on the Seebeck effect in thermoelectric materials such as PbTe and Bi_2Te_3 (3,4). When a thermal gradient is placed over a thermoelectric material, mobile electronic charge carriers (electrons or holes) diffuse from the hot side to the cold side of the material. Placing p and n-type elements thermally in parallel and electrically in series results in a thermoelectric couple, as shown in Figure 1.A. Such thermocouples can deliver power to an external load as long as a thermal gradient is present. The performance of thermoelectric devices is captured by the so-called figure of merit, ZT, as given by Equation 1 below (3,4). Here, S is the Seebeck coefficient, i.e. the measured potential difference per degree temperature difference. σ represents the electronic conductivity, κ is the thermal conductivity, and T is the operating temperature.

$$ZT = \frac{S^2 \sigma T}{\kappa} \tag{1}$$

This metric provides a guideline for optimizing thermoelectric materials and devices. More specifically, it is clear from this expression that to increase the figure of merit, a combination of low thermal conductivity and high electrical conductivity is desired. However, it is difficult to optimize both of these parameters simultaneously as the former is typically associated with insulating materials while the latter is most often found in metals – instead, a comprise is usually necessary (3,4). Furthermore, the figure of merit scales quadratically with the Seebeck coefficient, while typical thermoelectric materials possess comparatively low temperature coefficients on the order of 0.25 mV K^{-1} (5). For this reason, alternative harvesting strategies that may provide higher temperature coefficients are increasingly investigated. Note that in the following, we will use "temperature coefficient" as a generalized term to indicate the measured potential change to an

applied temperature fluctuation in any heat-to-electricity conversion device. In the case of a thermoelectric material, the temperature coefficient is a Seebeck coefficient as it is the Seebeck effect that is responsible for the potential-temperature coupling.
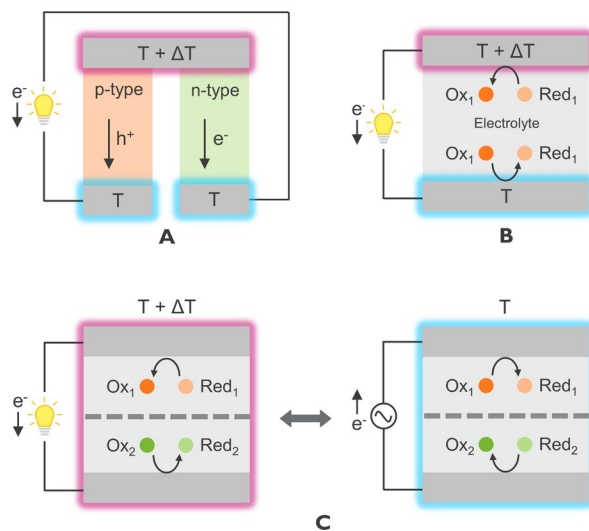
Figure 1. Overview of heat-to-electricity harvesting strategies. (A) Thermocouple based on thermoelectric materials: electrons or holes diffuse from the hot to the cold side, resulting in electric power generation. (B) Thermogalvanic cell: a temperature difference between two identical electrodes causes a reduction reaction at one electrode and the inverse oxidation reaction at the other, powering an external load. (C) Thermally regenerative electrochemical cycle: an electrochemical cell with two different half-reactions is discharged at a high temperature and charged at low temperature. When the cell potential is higher at high temperatures, net energy generation occurs.

One such approach is based on the thermogalvanic effect. Thermogalvanic cells contain two identical electrodes in contact with a common redox electrolyte. When a temperature difference is applied over the cell, a potential difference develops between the two electrodes. As shown in Figure 1.B, connecting the electrodes together results in reduction at the more positive electrode

and oxidation at the other side, generating power. Thermogalvanic cells can have significantly higher coefficients than thermoelectric materials: recent work has mainly focused on the $[Fe(CN)_6]^{3-/4-}$ redox couple, which provides high coefficients on the order of 1.4 mV K^{-1} (6–12). The origin of the thermogalvanic effect is the temperature dependence of the equilibrium potential U_{eq}, giving a thermogalvanic coefficient α that is in the simplest case given by Equation 2.

$$\alpha = \frac{\Delta U}{\Delta T} = \frac{\Delta S_{r,half-reaction}}{nF} \tag{2}$$

In this equation, $\Delta S_{r,half-reaction}$ represents the reaction entropy of the half-reaction, n is the number of electrons exchanged and F is the Faraday constant. However, in addition to the reaction entropy contribution of Equation 2, the actual measured coefficient in these symmetric cells can be affected by thermoelectric contributions of the electrode materials and the influence of thermodiffusion or the Soret effect, where the diffusive response differs for different ions in the thermal gradient over the electrolyte (5,6,13–15). Progress has recently been made in producing quasi-solid state thermogalvanic cells by using gel electrolytes, which could enable applications such as body-heat harvesting (11,12,16). However, thermogalvanic cells still suffer from large internal resistances that limit their output power, stemming from processes including Ohmic drop, charge transfer and mass transport limitations (6,17,18). In tandem with a low conductivity factor (19), these losses limits their usefulness for real-world systems.

For this reason, an alternative way of exploiting the thermogalvanic effect has recently been investigated. Thermally regenerative electrochemical cycles or TREC make use of an electrochemical cell with two different half-reactions occurring at either electrode, separated by a membrane. This cell is then charged and discharged at different temperatures, as shown in Figure 1.C. Since the cell potential is temperature-dependent, discharging at a temperature where the cell potential is higher results in net energy generation during this cycle (20–28). TREC cells can also

be made to operate autonomously, i.e. without the need of an external charging source, by intelligent material or cell selection (26,28). In analogy with Equation 2, the thermogalvanic cell coefficient of such a TREC device α_{cell} can be defined according to Equation 3, where α_1 and α_{2-} represent the individual thermogalvanic coefficients of the half-reactions respectively. In this equation, $\Delta S_{r,cell\ reaction}$ represents the full cell reaction entropy (22,24,26,27).

$$\alpha_{cell} = \alpha_1 - \alpha_2 = \frac{\Delta S_{r,cell\ reaction}}{nF} \tag{3}$$

Where both thermal and ionic conduction scale with intra-electrode separation in a thermogalvanic cell, the homogenous temperature distribution in a TREC cell makes it easier to optimize its internal resistance (19,23,24). Aside from ensuring electrode reversibility and cyclability, the most important parameters to obtaining a performant TREC system (i.e. high energy density and harvesting efficiency) are a high cell coefficient (19,23–25,27,29), low internal resistance (22,23,25,27), high specific electrode capacity (23–25), low volume of inactive components (19,27), and low heat capacity (19,23–25,27). The latter two parameters are especially far from optimized in current TREC systems: the presence of membranes or separators increases the mass of inactive components, and the use of liquid or gel electrolytes additionally increases the heat capacity of the system (20–28).

One especially interesting route that could be considered for improving TREC performance is to use thin-film Li-ion batteries. Indeed, Li-ion active electrode materials in general have excellent cyclability and very high energy densities (30,31). A proof-of-principle for Li-ion based TREC cells has already been demonstrated using standard slurry-coated composite electrodes with powder-based active material. However, the substantial volume of the separator and electrolyte in this configuration severely impacted the system performance (28). Solid-state thin-film batteries, which are today used for microstorage devices (32–37), contain solid electrolytes with very limited

absolute volumes and low heat capacities. This architecture is very suitable for creating high-performing TREC devices. Additionally, these components could provide significant advances in the integration and scalability of TREC systems – especially interesting in the context of powering IoT is their compatibility with vacuum processing techniques (32,34,38,39), which could eventually even enable on-chip harvesting.

The present work aims to address a major difficulty in designing and implementing thin-film Li-ion stacks in TREC systems: current information about the thermogalvanic coefficients of Li-ion electrodes is limited, and reliable methodologies for characterizing these coefficients are presently lacking. A few thermogalvanic cells featuring Li-ion electrodes have been constructed, which clearly demonstrated the thermogalvanic coefficient's dependence on the electrode lithiation state (5,40). The thermogalvanic cell coefficient for a single state-of-charge was also determined in coin cells by bringing the entire cell to different temperatures and measuring the resulting output potential change (5). In fact, the latter approach is experimentally identical to the determination of entropy profiles of bulk Li-ion batteries (41–48). These profiles have mainly been used as a tool to understand the thermal behavior of batteries or monitor the degradation of cells. In essence, Equation 3 is used to calculate the entropy change associated with the cell reaction from the thermogalvanic cell coefficient at various lithiation states. In what follows, we will refer to the dependence of a full Li-ion cell's thermogalvanic coefficient on the lithiation state as an entropy profile in accordance with Equation 3, since these quantities are linearly related. Likewise, the dependence of the thermogalvanic coefficient of a single electrode on the lithiation state following Equation 2 will be referred to as a thermogalvanic profile. When using lithium metal as a reference electrode, this reference electrode provides a constant contribution to the reaction entropy independent of the lithiation state, and the trend in the cell's entropy profile should only reflect the

working electrode's thermogalvanic profile. Such trends have then often been correlated with the phase behavior of the working electrode material (42,43,47,48). It has also been suggested that thermogalvanic profiles of Li-ion electrodes can vary with particle size (42). Indeed, for characteristic dimensions on the order of 100 nm or smaller, it is known that the phase behavior of Li-ion materials can differ significantly from the bulk case due to strong influences of nanoscaling effects (49–54). Thin-film electrodes have previously been used as a model system to study such nanoscaling effects (38).

The experimental methodologies that have been used in previous works are not appropriate as screening tools for the thermogalvanic profiles of individual Li-ion materials. Two types of approaches can be distinguished for this purpose: those based on entropy profiles, and those using thermogalvanic cells. Entropy profile measurements are executed using two-electrode battery cells with a lithium electrode. Using an electrochemical procedure, the lithiation state of the working electrode can be easily changed. During these lithiation steps, the lithium electrode is used as counter electrode. When measuring the entropy change via the thermogalvanic cell coefficient, the lithium electrode constitutes the reference electrode. Thermogalvanic cell coefficients determined from entropy profiles are reliable, as no thermoelectric or Soret interferences are present. However, this approach is not convenient as a screening tool for individual electrode materials: the electrode cannot be investigated by itself, but a new battery cell featuring the material to be studied as a working electrode must be built. In certain cases, the electrode material could be modified by these extra processing steps (55), potentially altering the measured profile.

A second existing option for thermogalvanic profile characterization is to use a thermogalvanic cell as shown in Figure 1.B. This approach is much more convenient, as it allows to study individual electrode materials. However, there are two significant issues with using

thermogalvanic cells to quantitatively measure the thermogalvanic profile of Li-ion materials. First, recall that thermogalvanic cells can include Soret and thermoelectric contributions. Soret contributions, though their exact magnitude cannot always be determined, are independent of the lithiation state (5). This merely results in a constant background contribution to the thermogalvanic profile, just as the reaction entropy of the lithium reference electrode in an entropy profile. However, thermoelectric contributions are more problematic. When placing powder-based electrodes in a thermogalvanic cell, an unknown portion of the temperature gradient falls over the electrode thickness (5). The lateral temperature distribution inside the electrode material may also be non-uniform, as effective electrode thickness varies significantly in powder-based architectures. As a result, thermoelectric interferences are created. Though the magnitude of these effects was previously measured to be limited (< 0.2 mV/K), they are influenced by the lithiation state of the electrode (5). Unlike Soret contributions, thermoelectric interferences can thus modify the measured dependence of the thermogalvanic coefficient on the lithiation state from what would be expected from Equation 2. Relying on such results for TREC design would clearly be inadvisable, as thermoelectric contributions do not occur in these devices.

The second and most crucial problem in using thermogalvanic cells for thermogalvanic profile measurements is that, to the best of our knowledge, this approach has never been used to determine thermogalvanic coefficients for Li-ion electrodes at electrochemically controlled lithiation states. Indeed, previous work using a thermogalvanic cell to show the lithiation state dependence of thermogalvanic coefficients in bulk electrodes employed prelithiated samples (5). Such a method is clearly not appropriate for collecting thermogalvanic profiles with high resolution: as each point of the profile necessitates the fabrication of separate samples, practical considerations limit the number of sampled points in the profile (e.g. only 5 lithiation states could be studied in the

aforementioned report (5)) and the investigation of fine profile features is thus prohibited. This limited resolution is especially problematic for the detection of possible nanoscaling effects. The accuracy of such a methodology is also not convincing: cross-sample variation between the samples used to probe different lithiation conditions could impact the resulting thermogalvanic profile trends and certainly leads to a significant uncertainty – standard deviations on the order of or greater than 0.1 mV K^{-1} were not uncommon in this report (5).

The thin-film electrode material selected for thermogalvanic characterization in the present work is anatase TiO$_2$. As mentioned above, it is known that many thermogalvanic profile features correlate with electrode phase behavior, and the well-understood phase transitions that anatase TiO$_2$ undergoes upon Li$^+$ insertion thus make it a well-suited model system. Various TiO$_2$ compounds have been investigated as Li-ion active materials, but the anatase polymorph remains among the most common (56). Anatase TiO$_2$ undergoes a Li$^+$ insertion reaction around 1.8 V vs Li$^+$/Li that is associated with the reduction of Ti(+IV) to Ti(+III) according to Equation 4. However, the theoretical capacity corresponding to x = 1, i.e. a full reduction of Ti(+IV) to Ti(+III) cannot be reached in bulk anatase TiO$_2$ due to limited ionic diffusivity for x > 0.6 (57). For this reason, various strategies have been investigated to enhance the insertion capacity of anatase TiO$_2$, including nanoscaling, doping, and forming composites (56,58,59).

$$TiO_2 + x\,Li^+ + x\,e^- \leftrightarrow Li_x TiO_2 \tag{4}$$
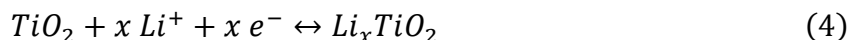
Anatase TiO$_2$ accommodates small amounts of Li$^+$ (x < 0.03) interstitially into its tetragonal crystal structure as an intercalation compound, i.e. without phase conversion. However, upon further Li$^+$ insertion, a biphasic transition occurs: a new orthorhombic lithium titanate phase with approximate composition Li$_{0.5}$TiO$_2$ forms and coexists with the remaining tetragonal anatase TiO$_2$ (53,60–63). In small particles, a second biphasic transition between this lithium titanate and a poorly-conductive tetragonal Li$_1$TiO$_2$ phase can occur (53,57,62). It is especially significant that

these phase transitions have been demonstrated to be highly susceptible to nanoscaling effects. More specifically, in addition to influencing the compositional limits of coexistence, decreasing the particle size has been shown to induce both aforementioned transitions to switch from a morphology of intra-particle coexistence to one where each particle supports only one of the two possible phases (53,61,63).

In this work, we developed a novel methodology for characterizing the thermogalvanic profile of Li-ion materials using an electrochemically-controllable thermogalvanic cell with thin-film electrodes. Electrochemical control was achieved using lithium ribbons that can serve as external reference and counter electrodes. In addition, the use of thin-film electrodes prevents thermoelectric interferences inside the electrode material from influencing the measured thermogalvanic profile trends. Crucially, the full thermogalvanic profile is measured iteratively on a single set of samples: this ensures cross-sample variability does not influence the thermogalvanic profile trends. Our approach turns out to be very powerful as we were able to determine thermogalvanic coefficients with a high degree of precision and could easily collect profiles with a lithiation state resolution of 5 %. The developed methodology was used to determine the first thermogalvanic profile of a thin-film Li-ion electrode, anatase TiO_2. This profile was demonstrated to be fully consistent with established phase behavior for this material, thus proving the methodology's validity. In fact, it was even possible to identify nanoscaling effects in the thermogalvanic profile. In the future, the methodology developed in this work could be used for additional studies into the thermogalvanic profiles of Li-ion materials, which could ultimately enable high-performing harvesting devices for the Internet-of-Things.

2. Experimental section

2.1. Electrode deposition and characterization

The TiO$_2$ thin films were deposited using an ALD process in a Pulsar 3000 reactor (ASM) at 250°C. Ti(OCH$_3$)$_4$ (titanium methoxide) was used as a Ti precursor and ozone as an oxidizing agent, and 750 cycles were executed for a target thickness of 40 nm. These depositions were performed on 300 mm Si wafers containing either a 100 nm SiO$_2$ layer (for Rutherford Backscattering Spectroscopy (RBS) and ellipsometry measurements) or a 30 nm TiN layer on top of a few nanometers chemical silicon oxide (for electrochemical and X-ray diffraction measurements). Thickness measurements of the TiO$_2$ layers were performed using SEM and spectroscopic ellipsometry mapping on a KLA Tencor SCD100 tool. The ellipsometry measurement was executed at an incident angle of 72°, and both the SiO$_2$ and the TiO$_2$ layers were fit with a harmonic oscillator model. Structural characterization was performed with grazing-incident X-ray diffraction (GI-XRD) on an X'Pert Panalytic tool with a Cu Kα source ($\lambda = 0.154$ nm) and an incident angle of 1°. The additional experiment of Figure 10 was executed in a Bruker D8 Discover XRD system with a Cu Kα source ($\lambda = 0.154$ nm) in an inert He environment using a conventional theta-two theta configuration (i.e. without grazing incidence). Peak assignment was performed using the X'Pert Highscore software. The total titanium content of the deposited TiO$_2$ films was determined with RBS. An incident beam of 40 nA He$^+$ with a 1.532 MeV beam energy was used. The analysis was performed using in-house software. The uncertainty in the RBS analysis is the sum of the counting statistical uncertainty and systematic errors. Systematic errors include uncertainties in the beam energy, detector energy calibration, measurement geometry, fitting algorithms, and uncertainties in the tabulated stopping powers. Elastic Recoil Detection (ERD) was used to determine the Li:Ti ratio in the lithiated films. This measurement was

conducted with a $^{35}Cl^{4+}$ primary ion beam accelerated to 8 MeV by a 2 MV tandem accelerator. A Time of Flight-Energy (ToF-E) telescope was used to detect forward recoiled and scattered ions. This telescope was installed at a forward scattering angle of 40° and had a length of 755.4 mm. All the elements were quantified using the recoil signals. The lithium signal was deduced from ^7Li and corrected with its natural abundance.

2.2. Electrochemical measurements

A custom-built Teflon cell was used for the electrochemical thermogalvanic measurements. This cell was designed in Autodesk Fusion 360 and fabricated in the in-house mechanical workshop. As indicated in Figure 2, it is based on a symmetric design: two identical thin-film electrode samples were placed on either end of the Teflon cell that was filled with a liquid electrolyte. By imposing a temperature difference between the samples while measuring the potential difference between them, the thermogalvanic coefficient could be determined. A DuPont Kalrez O-ring prevented electrolyte leakage, and the sample area exposed to the electrolyte on either side was 0.785 cm^2. All electrochemical measurements were executed with a 0.94 M $LiClO_4$ in propylene carbonate (PC) electrolyte. This solution was prepared by dissolving 10 g of $LiClO_4$ (battery grade, dry, 99.99%, Sigma Aldrich) in 100 mL of PC (anhydrous, Sigma Aldrich). To prevent contamination by moisture from air, the electrolyte was prepared and kept in an Ar filled glovebox. The assembled electrochemical cell was operated inside this glovebox as well.

Each sample was placed with its silicon substrate side on one side of a copper interposer with high thermal conductivity. The other side of the interposer was attached to a thermoelectric element (model APH-127-10-25-S, European Thermodynamics), which was used to set the temperature of the interposer to the desired value. Pt100 temperature sensors (model 891-9148, RS PRO) were placed close to the thermoelectric elements on the outside of the thermal interposer.

These class A temperature sensors have a tolerance of 0.19°C at 20°C – all temperatures mentioned in the following thus have an uncertainty of approximately ±0.19°C. As discussed in the SI, a thermal simulation showed that the temperature recorded by the sensor closely approximates the actual temperature of the sample. The minimal temperature that could be reached for each interposer with sufficiently large heatsinks for the thermoelectric elements was 15°C, and a maximum temperature of 55°C could be obtained. To prevent thermal leakage to the glovebox floor, the cell was operated on a thermal insulation pad. The actuation of the thermoelectric elements in this cell was executed by a thermoelectric controller (Meerstetter Engineering TEC-1122-SV). Custom Python software to apply predefined thermal programs to the cell via this controller was developed building on the Python implementation of the mecom protocol (pyMeCom) available on Github (64). Electrochemical data collection was performed with a Metrohm Autolab PGSTAT101 potentiostat running Nova 2.1 software.
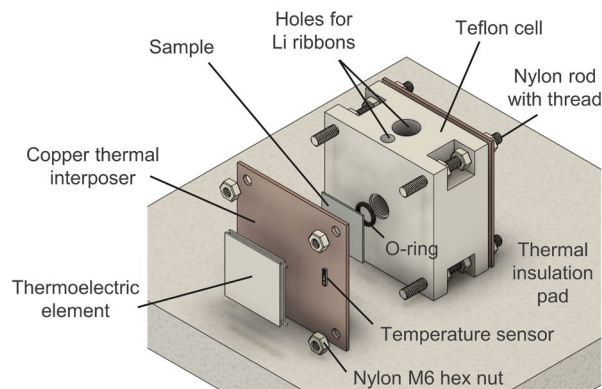
Figure 2. Schematic drawing of the electrochemical cell used for thermogalvanic measurements

The overall dimensions of the Teflon cell were 40 by 80 by 80 mm. On one side of the Teflon cell, a small vertical hole ($\emptyset$=7.5 mm) was provided for a lithium ribbon reference electrode. Additionally, a lithium ribbon counter electrode could be placed in the larger ($\emptyset$=15 mm) central

vertical hole in the cell. Using these lithium reference and counter electrodes, the lithiation state of the thin-film active material working electrodes was adjusted using a 3-electrode cell configuration. At each lithiation state, the thermogalvanic coefficient was determined from the potential difference when applying a set temperature difference between the electrodes. As such, the working electrode and reference electrode terminals of the potentiostat needed to be connected to different electrodes in the cell at different stages in the measurement procedure.

Synchronization between the thermal actuation and the electrochemical procedure on the one side, and potentiostat terminal switching on the other, were automated using a home-built switchbox module containing an Arduino Uno Rev3 SMD developer board and a four-way switchable mechanical relay module (BerryBase HLRELM-4). The Arduino module was addressed by the custom Python software that also controlled the thermal actuation using the Pyfirmata package. The Python-controlled Arduino module, cell electrodes, and potentiostat terminals were all coupled to the relay module to allow electrode switching. Finally, the Arduino module was also connected to the potentiostat to allow detection of DIO signals that can be sent from the potentiostat hardware during specified points in the electrochemical measurement procedure using the Autolab control command in Nova. These signals were used to establish a master-slave protocol for synchronization involving the electrochemical procedure (master) and the Python software (slave). In this way, thermal actuation and electrode switching occurred at the appropriate times during the measurement.

3. Results/Discussion

3.1. Physical characterization of electrodes

A tilted SEM image was collected to evaluate the morphology of the TiO_2 films deposited on 30 nm TiN-covered silicon substrates, as shown in Figure 3.A. From this image, it is clear that the

TiN is fully covered by a uniformly thin and continuous TiO_2 layer. In the inset of this figure, a cross-sectional SEM image is also shown. Here, the contrast between the TiN and TiO_2 layers was enhanced by using the element-sensitive backscattered electron detector. TiN shows up more brightly than TiO_2 in this image as it has a higher mass density, leading to more bright contrast-producing Ti atoms per cross-sectional area. Using the TiN layer with a known thickness of 30 nm as an internal reference, the TiO_2 layer has an apparent thickness of 35.7 nm.
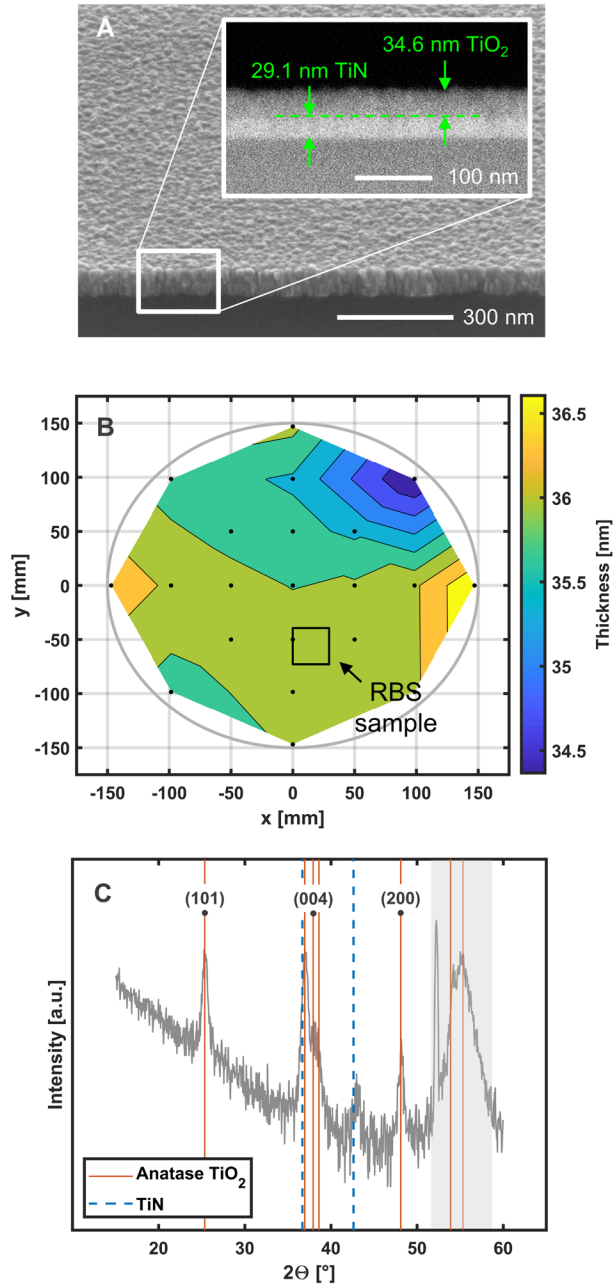
Figure 3. Physical characterization of anatase TiO$_2$ thin films. (A) SEM image of TiO$_2$ films deposited on a 300 mm Si wafer with 30 nm TiN. (B) Spectroscopic ellipsometry thickness mapping of TiO$_2$ films deposited on a 300 mm Si wafer with 100 nm thermal SiO$_2$. The approximate location of the sample used in the RBS analysis is indicated with a square. (C) XRD spectrum of TiO$_2$ films deposited on a 300 mm Si wafer with 30 nm TiN. The blue dotted lines

correspond to signals from the TiN substrate while the solid orange lines indicate anatase TiO_2 peak locations.

The thickness uniformity of the deposited TiO_2 films across the 300 mm wafers was mapped using spectroscopic ellipsometry as shown in Figure 3.B. The average thickness of the TiO_2 layer was 36.1 nm, in close agreement with the SEM result. The cross-wafer spread was approximately 2.6 nm or 7.1 %. The ellipsometry goodness-of-fit (R^2), which reflects the uncertainty on the obtained thicknesses, was > 0.986 over the full wafer. From this wafer, a representative sample was taken for RBS analysis. The location of this sample on the wafer is indicated in Figure 3.B. Using RBS, the total Ti content of the TiO_2 thin film was determined to be $105.3 \cdot 10^{15}$ Ti atoms cm^{-2}, with a total uncertainty of $2.6 \cdot 10^{15}$ Ti atoms cm^{-2}. As anatase TiO_2 can theoretically insert up to 1 mol Li^+ per mol Ti, this gives a theoretical lithiation capacity of $4.69 \pm 0.16 \cdot 10^{-6}$ Ah cm^{-2}. From the ellipsometry results, the thickness of the RBS sample was determined to be 36.1 nm at this particular spot. Using a molar mass of 76.865 g mol^{-1} for TiO_2, a film density of 3.72 ± 0.09 g cm^{-3} was calculated. This is close to the theoretical mass density of 3.84 g cm^{-3} (65), confirming the dense and smooth nature of the deposited films.

Finally, the structure of the as-deposited TiO_2 films was measured using GI-XRD, as indicated in Figure 3.C. The peaks from 52-57° (indicated in the grey box in Figure 3.C) are introduced by the Si substrate, while the peaks corresponding to the dashed blue lines can be attributed to the TiN layer (JCPDS file 71–0299). There is excellent agreement between the observed spectrum and the expected peak locations of the anatase TiO_2 polymorph (JCPDS file 02-0387) shown with solid orange lines in Figure 3.C. This agreement indicates that the deposited film is polycrystalline and has the anatase structure, with the (101), (004), and (200) reflections at 25.4°, 37.9° and 48.1°

respectively as the most prominent peaks. Using the Scherrer equation for the (101) peak, a rough estimate of 13 nm was obtained for the particle size.

3.2. Methodology development

As discussed previously, current methodologies are unsuitable as screening tools for thermogalvanic profiles of Li-ion materials. The development of a new and performant measurement methodology based on a symmetric thermogalvanic cell is presented below. Our method features two novel elements. First, the electrode materials are studied in thin film form. The thickness of the Teflon cell over which temperature differences are applied is 4 cm, while the electrode material thickness is only approximately 36 nm. We thus do not expect temperature differences inside the thin-film electrodes to be significant in our measurements. As such, thermoelectric contributions should not influence the thermogalvanic profiles measured with this methodology. Additionally, the developed methodology makes use of electrochemically-controllable lithiation states via the inclusion of lithium ribbons that can serve as external reference and counter electrodes. This allows the measurement of the entire thermogalvanic profile on the same set of samples. In this way, cross-sample variation effects do not impact the profile, and high lithiation state resolution is possible.

In the following, we will first elaborate on the measurement protocol that was developed. Next, it will be shown how the experimentally sampled potential and temperature data can be translated into a thermogalvanic profile. Finally, the robustness of the method is considered by evaluating the effect of sample and thermal program variations.

3.2.1 Experimental protocol

The experimental protocol for collecting the thermogalvanic profile is illustrated schematically in Figure 4 below. During the measurement, the potentiostat terminals were connected to different

electrodes in the cell via the action of the relay module in the switchbox. More specifically, two electrode configurations were used. In configuration A, lithium ribbons were used as the counter and reference electrodes, while the electrode samples were shorted together and connected to the working electrode terminal of the potentiostat. In this manner, the two electrodes were charged or discharged the same amount when a certain current or potential was applied. Configuration A was used for the initial steps in the experiment, i.e. applying 3 cycles of cyclic voltammetry and galvanostatically lithiating and delithiating both samples between 0.5 and 3.0 V vs Li^+/Li for anatase TiO_2. These initial operations ensured that any first-cycle effects were avoided in the subsequent thermogalvanic profile determination.
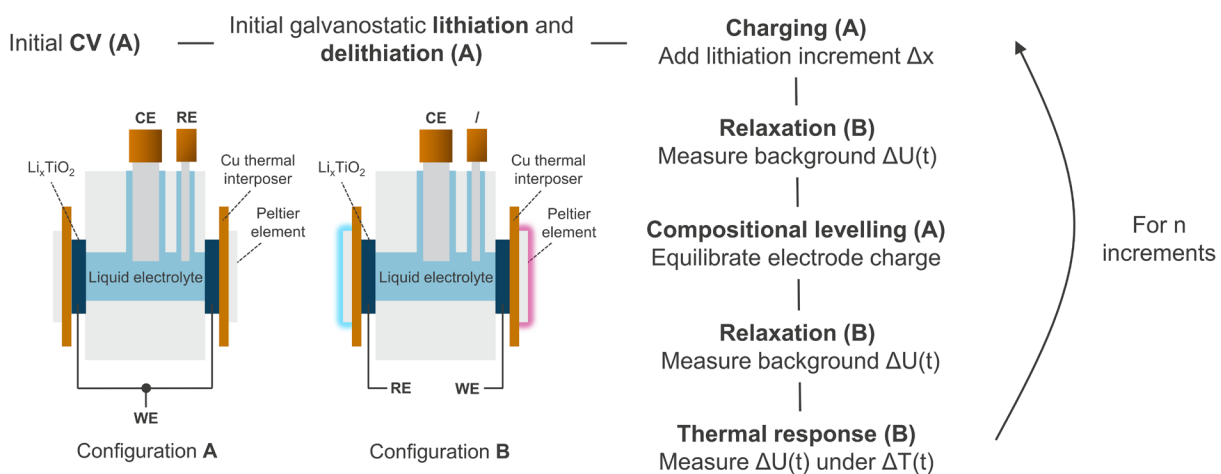
Figure 4. Schematic overview of the protocol for thermogalvanic profile determination. The thermogalvanic profile is determined iteratively by adding a charge increment and measuring the thermal response for n points in the profile. Two cell configurations are used: one for setting the lithiation state of both electrode samples (configuration A) and one for measuring the potential difference ΔU between these electrodes either with or without a temperature difference ΔT (configuration B). WE, RE, and CE represent the working, reference, and counter-electrodes, respectively.

20

After these initial steps were completed, the iterative part of the measurement during which the thermogalvanic profile is recorded commenced. First, a charge increment was galvanostatically added to both electrodes while still using configuration A. Once the new lithiation state had been reached, the electrode connections were switched to configuration B. In this configuration, the potential difference between the samples could be measured as the electrode samples were no longer shorted. Instead, one of them was connected to the potentiostat working electrode terminal while the other was connected to the reference electrode terminal. A lithium ribbon was still used for the counter electrode.

Once in configuration B, the system underwent a relaxation step of 30 minutes. During this step, the potential difference between the samples was monitored at a constant temperature of 25°C, i.e. in the absence of a temperature difference. This background potential difference should be small (< 1 mV) to ensure that no background effects interfere with the subsequent thermal response measurement. After the relaxation step, the thermal response was determined: the potential difference between the electrodes was measured while the temperature difference between them was changed via the thermoelectric elements with a predetermined thermal program. The thermal response measurements in this work had a duration between 30 and 50 minutes. From the thermal response, the thermogalvanic coefficient at this lithiation state could later be determined. Once this thermal response had been collected, the electrode configuration was switched back to condition A, and a new charge increment was applied. This process continued iteratively until all n desired lithiation states in the thermogalvanic profile had been probed.

As will be discussed later, it was observed that a small charge inequality could be present between the electrodes. As this effect interfered with an accurate determination of the thermogalvanic coefficient, it was necessary to include a compositional levelling step before the

thermal response was determined. In this step, the two electrode samples were once again shorted together using configuration A, but no current was applied: this allowed charge equilibration between the samples. Compositional levelling was allowed to proceed for 1 hour. After the levelling step, configuration B was again used to determine the background potential difference with a second 30-minute relaxation step. The final potential difference after this last relaxation step was never greater than 1 mV in all measurements, indicating good charge state similarity between the electrode samples after compositional levelling.

3.2.2 Thermal response distortions

The thermal response measurement forms the last step in the iterative block of the measurement protocol. During this thermal response determination, the temperature difference between the samples is changed while the potential difference is recorded. The goal is to then extract a thermogalvanic coefficient from this thermal response. Figure 5 shows a typical example of a thermal response recorded in thin-film anatase TiO_2 with the methodology developed in this work. In this Figure, a close relation between the measured potential difference and the temperature difference can be observed, as expected for a thermogalvanic cell. The potential difference mostly follows the imposed temperature difference, both in sign and magnitude. However, the measured potential difference does not scale one-to-one with the temperature difference. Two types of distortions with respect to this one-to-one scaling can be observed. First, the potential difference does not return to zero when the temperature difference is removed, which will be referred to as baseline drift. Secondly, peak drop-off is observed: the peak in the potential difference starts decreasing before the temperature difference has reached its maximum. As the severity of these distortions was observed to vary with the lithiation state of the electrodes, they are unlikely to be caused by a Soret phenomenon, which should produce the same effect independent of the electrode

lithiation state. Though these artefacts appeared puzzling at first, we were able to explain them as

a consequence of small amounts of leakage through the electronics used in the setup. During the

potential measurement, a small electronic leakage through the external circuit still leads to slow

charge/discharge between the samples which are at different potentials. This leakage effect can

result in charge inequalities between the electrode samples which manifest as peak drop-off and

baseline drift in the thermal response measurements.
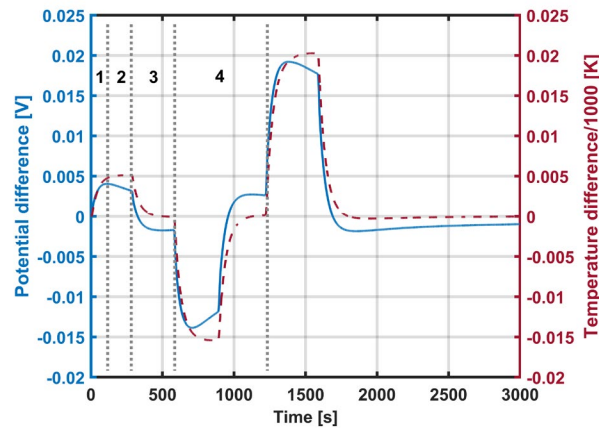
Figure 5. Typical example of a thermal response collected using the developed methodology on

thin-film anatase TiO_2 electrodes. Left axis: measured potential difference as a function of time.

Right axis: corresponding applied temperature difference scaled by a factor 1000. Temperature

difference regions 1-4 correspond to 1) increasing temperature difference for t = 0-100 s; 2)

constant temperature difference for t = 100-300 s; 3) removal of temperature difference for t =

300-600 s; 4) application of temperature pulse with opposite sign than in regions 1-3 for t = 600-

1200 s.

To demonstrate this effect, the temperature difference regions labelled in the thermal response

in Figure 5 will be examined in detail. First, at time t = 0 s, the potential difference between the

samples was small due to compositional levelling. Between 0 and 100 s (region 1 in Figure 5), the

temperature difference between the electrode samples increased. At first, the potential difference between the hot electrode (connected to the working electrode terminal of the potentiostat) and the cold electrode (connected to the reference electrode terminal) increased along with the imposed temperature difference due to the thermogalvanic effect. Next, the temperature difference was maintained at a constant value between 100 and 300 seconds (region 2 in Figure 5). However, instead of also attaining a constant value, the potential difference started to decrease. This drop-off can be interpreted as a leakage effect. When the potential of the hot electrode increases relative to the cold electrode due to the thermogalvanic effect, there is a driving force for electrons and ions to move from the cold electrode to the hot electrode. Normally, electrons should not be able to transfer via the external circuit in case of a potential measurement. However, a normally negligible leakage current still causes a measurable change in lithiation state due to the small amount of active material in the thin films used here. This causes the potential difference between them to decrease, leading to the observed peak drop-off. The paths that may be responsible for this charge leakage are considered in more detail in a later section.

From t = 300 s to t = 600 s (region 3 in Figure 5), the temperature difference was removed, and the thermogalvanic potential difference dropped. However, the previously established charge difference did not disappear. Its enduring presence results in a nonzero potential difference after the temperature difference is removed, explaining the observed baseline drift. The difference in the potential baseline value before (i.e. at t = 0 s) and after the temperature pulse (i.e. at t = 600 s) reflects the charge that was transferred as the result of leakage during this first pulse. In the next temperature pulse (t = 600 to 1200 s, region 4 in Figure 5), a temperature difference of opposite sign is applied. Since the potential difference now also has an opposite sign, charge leakage occurs in the other direction, leading to positive peak drop-off and baseline drift. The difference in the

value of the potential difference at the start (t = 0 s) and end (t = 3000 s) of the entire thermal response measurement reflects the net amount of charge that was moved due to the temperature pulses. To allow continued accurate determination of the thermogalvanic coefficient, care must be taken to remove this remnant charge difference before starting the next increment in the profile measurement. This can be achieved via compositional levelling.

When viewing the effects of peak drop-off and baseline drift as a consequence of charge leakage, the thermogalvanic response can be isolated by assuming the total measured potential difference to be a superposition of a thermogalvanic contribution and a charge inequality contribution. At the moment where the temperature difference is removed, the driving force for charge leakage disappears rapidly. The change in the potential difference from the value at the start of this drop (i.e. the corner of the potential difference signal) to the new potential difference minimum can thus be approximated as a purely thermogalvanic effect. This change in the potential difference is then divided by the value of the peak temperature difference to give the thermogalvanic coefficient. Using this approach, a thermogalvanic coefficient can be determined for each temperature pulse in the thermal response measurement. These coefficients are then averaged to obtain the thermogalvanic coefficient of the electrode at the selected lithiation state.

3.2.3 Compositional levelling

The use of a compositional levelling step is critical to obtaining a reliable value for the thermogalvanic coefficient over the entire course of the profile measurement. To illustrate this, two thermogalvanic profile measurements were executed; one with and one without compositional levelling, as shown in Figure 6. In the latter case, 1 h of compositional levelling was performed after every charging step and before the collection of the thermal response (see Figure 4). The data in Figure 6 was collected for 10 delithiation increments, with a current density of $1.55 \cdot 10^{-6}$ A cm$^-$

<superscript>2</superscript> applied for 473 s during each charging step. The thermal program was identical to the one indicated in Figure 5. Using the method described in the previous section, a thermogalvanic coefficient was calculated from the thermal response at every delithiation increment. This results in the thermogalvanic profiles in Figure 6, where the square markers show the average coefficient. Additional comments on the thermal responses are provided in the SI.
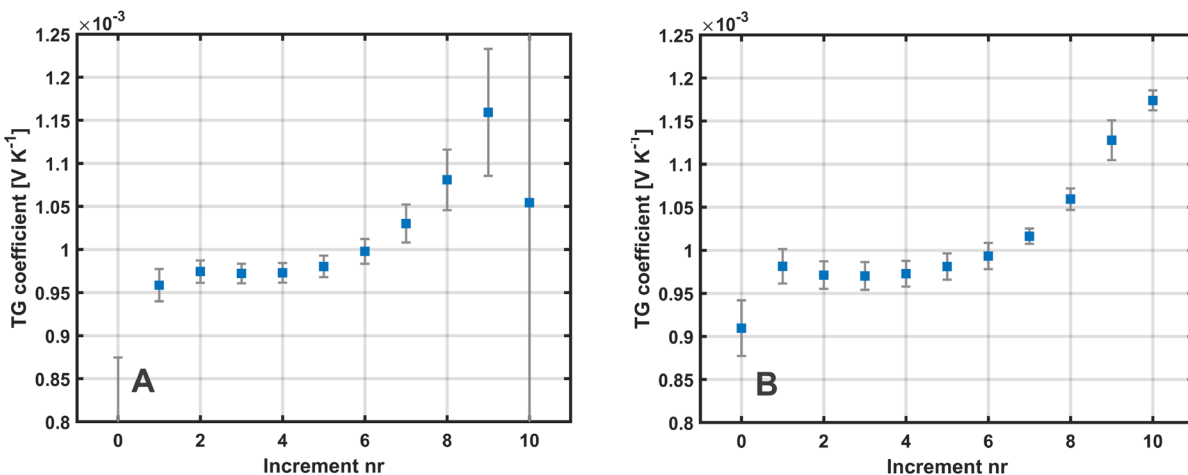
Figure 6. Thermogalvanic profiles measured on anatase TiO_2 thin-film electrodes without compositional levelling (left, A) and with 1 h compositional levelling before thermal response collection (right, B). 10 delithiation increments were sampled with a current density of $1.55 \cdot 10^{-6}$ A cm^{-2} applied for 473 s during every charging step. The same thermal program as in Figure 5 was used in all cases.

The error bars in Figure 6.A and Figure 6.B reflect the spread on the thermogalvanic coefficients obtained from different pulses, i.e. the difference between the greatest and the smallest calculated coefficient. This spread is a result of the charge leakage between the samples that occurs during the thermal response measurement. Since this leakage causes the two samples to have slightly different charge states, the thermogalvanic coefficient calculated for each temperature pulse is offset from the true value that would be obtained with both electrodes at the nominal lithiation

26

state of this increment. As every pulse induces a different charge difference and thus a different offset, averaging the coefficients calculated from temperature pulses of different magnitude and sign yields a value that approximates the true thermogalvanic coefficient.

When no compositional levelling is used, the remnant charge inequality present at the end of each thermal response measurement is not removed. This leads to the accumulation of a background charge difference over the progression of the experiment. Eventually, this background charge difference could become large enough that a fundamentally different thermogalvanic coefficient is expected for the two samples. The measured coefficient would then be some average of these two different values. However, even if that average value would be an acceptable approximation of the true thermogalvanic coefficient at the chosen nominal lithiation state, it is not possible to determine it with a high degree accuracy due to the significantly increased spread on the measured coefficient value. This increasing spread with measurement progression can be clearly observed from increment 7 onwards in Figure 6.A. The relationship between this increasing spread and the background charge difference is explained further in the SI. It is clear that this increasing spread greatly reduces the reliability of the measured thermogalvanic coefficients. As such, the use of a compositional levelling is of the utmost importance towards obtaining an accurate quantitative value for the thermogalvanic coefficient over the entire experimental lithiation range.

3.2.4 Estimation of potential difference due to charge leakage

To further confirm charge leakage between the samples as the origin of the distortions in the thermal response measurements, the net change in the potential difference between the samples that is expected as a consequence of such leakage is estimated. During these thermal response

measurements, one sample is connected to the working electrode terminal and the other to the reference electrode terminal. We can then define:

$$d\Delta U = dU_{WE} - dU_{RE} \tag{4}$$

Herein, ΔU is the measured potential difference, U_{WE} is the potential of the TiO$_2$ sample at the working electrode and U_{RE} is the potential of the TiO$_2$ sample at the reference electrode. Consider the application of a temperature pulse that increases the temperature of the working electrode sample with respect to the reference electrode sample. Due to the positive potential difference ΔU that develops as a result of the thermogalvanic effect (see Figure 5), there is a driving force for electrons and Li-ions to move from the reference electrode sample to the working electrode sample. As a consequence of this charge leakage, the working electrode sample would lithiate by a small amount dx, and the reference electrode sample would delithiate by the same amount. This results in Equations 6-7, where x represents the fraction of Li$^+$ in either electrode sample:

$$d\Delta U = \frac{\partial U_{TiO_2,lithiation}}{\partial x}dx - \frac{\partial U_{TiO_2,delithiation}}{\partial x}(-dx) \tag{6}$$

$$\frac{d\Delta U}{dx} = \frac{\partial U_{TiO_2,lithiation}}{\partial x} + \frac{\partial U_{TiO_2,delithiation}}{\partial x} \tag{7}$$

To estimate the dependence of the equilibrium potential of TiO$_2$ on the amount of Li, we can use the galvanostatic lithiation and delithiation curves determined at the start of the experimental procedure. However, it must be stressed that galvanostatic lithiation/delithiation curves are not always an accurate predictor of the thermodynamic property of lithiation-dependent equilibrium potential, as kinetic effects (which manifest as overpotentials) play a very significant role in these measurements.

The lithiation/delithiation curves determined at the start of the experiment with compositional levelling discussed previously are shown in Figure 7. As the current density used for initial lithiation/delithiation is the same as the current density in the charge increment steps, the charge

range in Figure 7 is the same as the summed increment range of Figure 6.A and B. In Figure 7, the lithiation and delithiation curves are plotted versus a common charge axis that is linearly related to the Li$^+$ fraction in the electrode. At the current density of $1.55 \cdot 10^{-6}$ A cm^{-2} that is used in this experiment, Li$^+$ could only be inserted up to x = 0.39, in accordance with the commonly accepted limited rate capability of TiO$_2$ (57). According to Equation 7, the expected change in the potential difference between the two TiO$_2$ samples due to a small amount of charge leakage is equal to the sum of the slopes of the discharge/lithiation and charge/delithiation curves (insofar as those can be used to estimate the respective derivatives in Equation 7). This net slope is calculated via numerical differentiation and plotted as a function of the charge state of the electrode on the left axis in Figure 7.
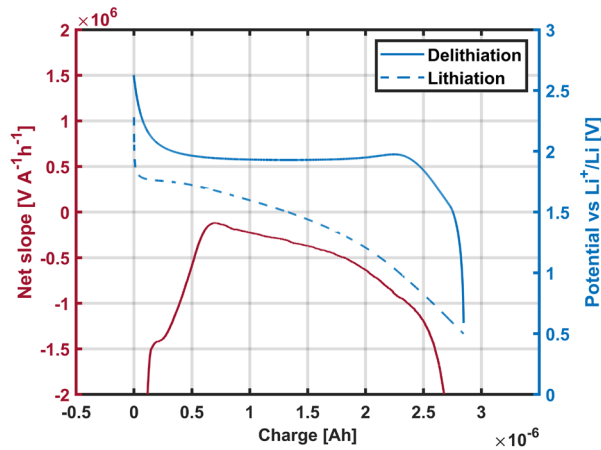
Figure 7. Right axis: initial galvanostatic lithiation (dashed line) and delithiation curves (solid line) collected on anatase TiO$_2$ thin-film electrodes during the experiment with compositional levelling of Figure 6.B. A current density of $1.55 \cdot 10^{-6}$ A cm^{-2} was applied to a 1.57 cm^2 electrode. The charge on the x-axis is directly proportional to the amount of Li$^+$ in the electrode. Left axis: net slope of delithiation and lithiation curves as a function of charge state.

As discussed in the SI, the charge dependence and sign of the net slope in Figure 7 are in accordance with the observed thermal response distortions. Most significant, however, is the magnitude of the net slope in Figure 7. Around the middle of the charge range considered here, this quantity reaches a value of approximately $-3 \cdot 10^5$ V Ah^{-1}. For the middle increment (i = 5) in the thermogalvanic profile with compositional levelling of Figure 6.B, a change in the baseline potential of 0.3 mV was observed in the thermal response measurement after a 600 s temperature pulse of +5°C. Via the net slope value, such a potential change would require the movement of $1 \cdot 10^{-9}$ Ah of charge. Over the duration of the temperature pulse, this implies an average current of 6 nA. Such small leakage currents can have observable effects in thin-film systems: small absolute amounts of charge significantly change the relative lithiation state and thus the potential of thin-film electrodes. The ionic component of this leakage current can occur via the liquid electrolyte in the cell. The electronic leakage path is less clear – we suspect the relay modules used in the switchbox for the experimental setup as a possible source. In any event, it must be emphasized that the value of the thermogalvanic coefficient can still be obtained with a very high degree of precision even with these small amounts of charge leakage, provided a compositional levelling step is used. To reduce the charge leakage-induced spread on the experimental data even further, a more sophisticated setup featuring dedicated low-leakage switching components could be considered in the future.

3.2.5 Effect of sample variation and thermal program

The final step of the methodology development is to ascertain that sample variations or the exact nature of the thermal program do not significantly influence the result of the thermogalvanic measurements. To this end, three thermogalvanic profiles were collected with compositional levelling and 10 delithiation increments of 473 s at $1.55 \cdot 10^{-6}$ A cm^{-2}, each using a different thermal

program. All three experiments were conducted on different sets of samples. Figure 8 illustrates these results – the inset of each plot shows the thermal program used in the associated experiment. The thermal program used in Figure 8.A is identical to that of Figure 5 (i.e. temperature differences of +10, -15 and +20°C) and serves as a point of comparison. By contrast, the program in Figure 8.B had a different number of thermal pulses than the original program and a different loading pattern featuring an additional large negative pulse at the end (i.e. temperature differences of +5, -5, +15 and -15°C). If the nature of the thermal program truly does not influence the measurement, the thermogalvanic profiles recorded with these two differing programs should yield quantitatively identical coefficients. Finally, the program used in Figure 8.C was similar to that of Figure 8.A, but with a thermal pulse magnitude half as large as in Figure 8.A (i.e. temperature differences of +2.5, -5 and +10°C). In addition to an identical average coefficient value, this program should also result in a smaller coefficient spread due to the reduced driving forces for spread-inducing charge leakage.

In Figure 8, the same qualitative dependence of the thermogalvanic coefficient on the charge state emerges regardless of the thermal program used. Small differences in this dependence between different experiments are likely a result of the thickness variation between different samples. As indicated previously, thickness variations on the order of 7 % are expected for these thin films. Such thickness differences lead to a slightly different theoretical capacity for each set of samples, resulting in different relative lithiation states for the same absolute amount of added charge during an increment. Still, for most increments in Figure 8, the variability of the thermogalvanic coefficient between different experiments is no larger than the spread on the thermogalvanic coefficient at this increment in each individual experiment. This spread is mostly

limited to 0.02 mV K^{-1} or about 2 %. Clearly, the developed methodology is quite robust to both

thermal program and sample variations.
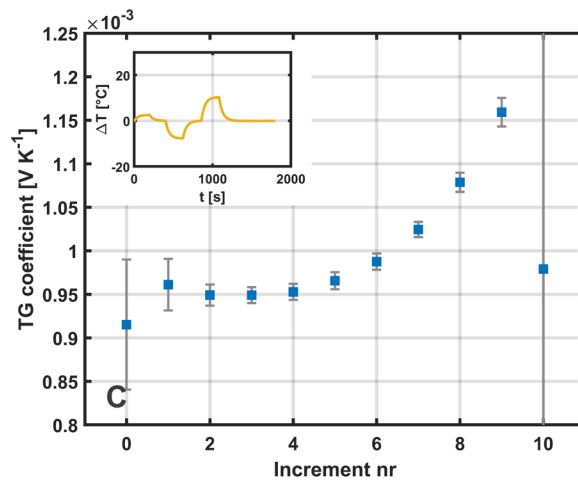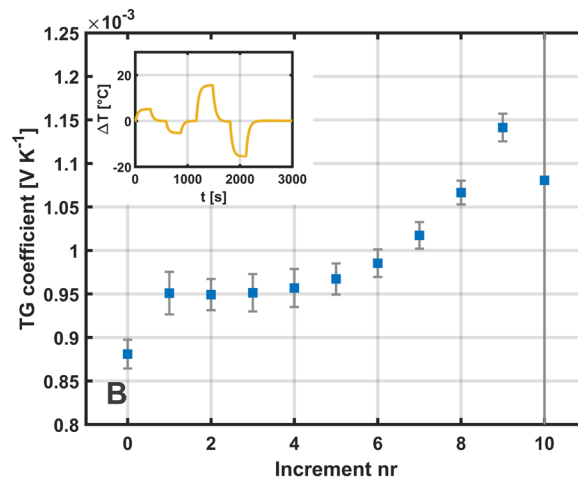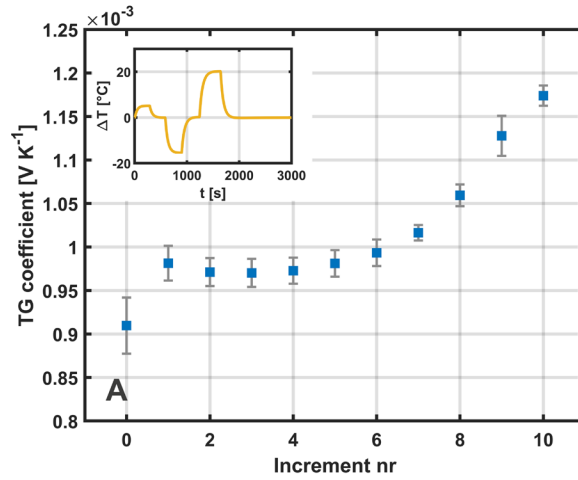
Figure 8. Thermogalvanic profiles of anatase TiO_2 thin-film electrodes collected with three different thermal programs. 10 delithiation increments were sampled with a current density of $1.55 \cdot 10^{-6}$ A cm^{-2} applied for 473 s during every charging step. (A) Thermal program as in Figure 5. (B) Full thermal inversion: temperature differences of +5, -5, +15 and -15°C. (C) Small amplitude thermal program: same pulse ratios as (A), but with magnitudes that are half as large.

Additionally, a standard deviation can be calculated from the average coefficients determined in each of these three experiments. When excluding increment 10, which is highly influenced by the small capacity differences between the samples, an average standard deviation of 0.01 mV K^{-1} is found over the sampled lithiation range. This metric can be compared to the standard deviations obtained in a previous study on the lithiation state dependence of thermogalvanic coefficients in prelithiated bulk electrodes. Over most of the studied lithiation range, this report obtained standard deviations that appear to be on the order of 0.1 mV K^{-1} for four experiments (5). This tenfold reduction in standard deviation clearly demonstrates that the methodology developed in the present work allows quantitative determination of the thermogalvanic coefficient with comparatively superior precision.

Finally, it is worthwhile to compare the spread on the thermogalvanic coefficients between Figure 8.C and the other two experiments. As stated above, the thermal program used in Figure 8.C had a smaller pulse amplitude than the other programs. It can be observed from Figure 8 that this small amplitude program results in a decreased spread on the measured thermogalvanic coefficient. This is in accordance with the previously discussed link between charge leakage and coefficient spread: smaller temperature differences result in smaller thermogalvanic potential differences and thus a smaller force for charge leakage. More limited charge leakage would result in smaller offsets from the true thermogalvanic coefficient value and thus a smaller spread, in

excellent agreement with Figure 8.C. In conclusion, the precision of the developed methodology can be even further increased by using thermal programs with small amplitudes.

3.3. Thermogalvanic profile of anatase TiO$_2$

Using the novel methodology presented above, the full thermogalvanic profile of the anatase TiO$_2$ thin films was determined. In this section, we will first discuss the physical principles that control thermogalvanic profiles. Next, the measured profile of anatase TiO$_2$ will be discussed, and we will demonstrate how this profile is completely in accordance with the established phase behavior of anatase TiO$_2$. Additionally, it will be shown that nanoscaling effects can be detected in the collected profile. In this way, the validity and strength of the developed approach is proven.

3.3.1 Principles of thermogalvanic profiles

Before analyzing the thermogalvanic profile of anatase TiO$_2$ in detail, we will first comment on the general principles governing the shape of these profiles. First, just as for entropy profiles, the coefficient value in a thermogalvanic profile cannot be directly translated into a reaction entropy for the electrode half-reaction via Equation 2 due to an offset. Whereas this offset is the reaction entropy of the counter electrode in an entropy profile, it arises due to various background contributions in a thermogalvanic cell measurement (5,13,14). However, as explained previously, these contributions are either not significant in thin-film electrodes (thermoelectric interferences) or independent of the lithiation state (Soret effect). As a consequence, the evolution of the thermogalvanic coefficient with lithiation state measured using our methodology is solely an effect of the electrode reaction entropy. This reaction entropy describes the change in the electrode molar entropy when the lithiation reaction proceeds by an incremental amount. It can also be described as a lithiation entropy or a partial molar entropy of Li$^+$ insertion (5). As such, it must be stressed that the thermogalvanic profile cannot be read as a reflection of the total molar entropy of the

electrode material. Instead, trends in the thermogalvanic profile indicate evolutions in the entropy change associated with incremental lithium insertion for varying lithiation conditions of the electrode. In other words, a nonzero slope in the thermogalvanic profile reflects that Li$^+$ insertion at a Li$^+$ fraction of x creates a different entropy change than lithium insertion at a Li$^+$ fraction of x + Δx.

As an example, consider the lithiation entropy in an electrode that behaves as a single-phase intercalation compound over a certain lithiation range. It has been established that the lithiation entropy of such compounds is often dominated by a configurational entropy that originates in lithium ion-vacancy disorder – i.e. the disorder induced by distributing x Li ions and (1 − x) Li vacancies over the intercalation material. This process is described by the ideal entropy of mixing, resulting in a lithiation entropy described by Equation 8 below where k_B is the Boltzmann constant and χ describes the relative extent of lithiation. The latter parameter is directly proportional to the Li$^+$ fraction, x, in the intercalation material (43). Equation 8 predicts a continuously decreasing lithiation entropy over the range available for Li$^+$ intercalation, in accordance with experimental observations for such systems (5,42,43). This signifies that incremental lithiation in a mostly depleted structure creates a larger entropy change than incremental lithiation in a partially filled structure.

$$\Delta S_{lithiation} = k_B \ln \left(\frac{1 - \chi}{\chi} \right) \tag{8}$$

In contrast, a plateau in the thermogalvanic profile reflects that the entropy change produced by lithiation does not vary over a certain composition range. Such behavior is to be expected for two-phase coexistence (42,43). For first-order phase transitions, the two phases involved have equal Gibbs free energy in the region of coexistence, and the total Gibbs free energy is thus constant.

According to Equation 9, the lithiation entropy is then also constant, resulting in a thermogalvanic coefficient that becomes independent of the lithiation state.

$$\frac{\partial \Delta S_{lithiation}}{\partial x} = \frac{\partial}{\partial x}\left(\frac{\partial \Delta G}{\partial T}\right) = \frac{\partial}{\partial T}\left(\frac{\partial \Delta G}{\partial x}\right) = \frac{\partial}{\partial T}(0) = 0 \qquad (9)$$

Finally, thermogalvanic profiles can also show sharp increases and decreases. These features often appear at well-defined compositions and are linked to phase transitions, such as the hexagonal to monoclinic back to hexagonal transitions around x = 0.5 observed in Li_xCoO_2 (43,48). In general, sharp increases have been correlated with the formation of a more disordered phase, while a transition to a more ordered state can produce a sudden decrease in the lithiation entropy (42).

3.3.2 Analysis of thermogalvanic profile trends in anatase TiO_2

Figure 9 shows the measured thermogalvanic profile of anatase TiO_2. This profile was determined using 20 lithiation increments and compositional levelling. The thermal responses were collected using the reduced amplitude thermal program of Figure 8.C. A lithiation increment current corresponding to a rate of C/4 was selected. This rate is referenced to the theoretical capacity determined by RBS, i.e. $4.69 \pm 0.16 \cdot 10^{-6}$ Ah cm^{-2}. The increment numbers in this measurement can then be matched to a Li^+ fraction in the electrode, i.e. an x value in Equation 4. When attempting to insert Li^+ past x = 0.65, the potential measured during the lithiation increment step dropped below 0 V vs Li^+/Li. This observation agrees with aforementioned limited rate capability of anatase TiO_2 which prohibits the material from reaching its theoretical capacity x = 1 under standard conditions (57). As such, it was not possible to determine a meaningful thermogalvanic coefficient for x > 0.65.
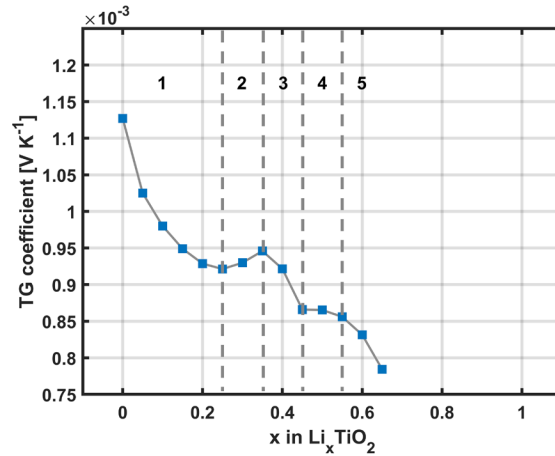
Figure 9. Thermogalvanic profile of a 36 nm anatase TiO₂ thin film collected using 20 lithiation increments of C/4 or $1.17 \cdot 10^{-6}$ A cm^{-2} with the low-amplitude thermal program of Figure 8.C. Five regions can be identified in this profile: 1) decrease for x = 0-0.25; 2) increase for x = 0.25-0.35; 3) decrease for x = 0.35-0.45; 4) plateau for x = 0.45-0.55; 5) decrease for x = 0.55-0.65.

Using the principles discussed above, we can now explain the trends in the thermogalvanic profile of thin-film anatase TiO₂ of Figure 9. As indicated in Figure 9, this profile can be divided into 5 regions. The first region of this profile spans the range between x = 0 and x = 0.25 and features a decreasing coefficient. For low degrees of lithiation, anatase TiO₂ is known to intercalate Li$^+$ into its crystal structure. Indeed, the continuously decreasing trend in this region is in accordance with the decreasing lithiation entropy expected for intercalation compounds, as explained previously.

The second region in the thermogalvanic profile covers approximately x = 0.25 to x = 0.35, where the thermogalvanic profile increases. Consider first the increase from 0.25 to 0.30, indicating that Li$^+$ insertion at a composition of x = 0.3 results in a greater entropy change than insertion at x = 0.25. For anatase TiO₂, higher amounts of Li$^+$ loading have been demonstrated to lead to two-phase coexistence between the anatase phase and a new orthorhombic lithium titanate

phase with approximate composition $Li_{0.5}TiO_2$. The latter will henceforth be referred to as the titanate phase. According to the discussion above, such coexistence should lead to a plateau in the thermogalvanic profile instead of an increase. However, this increase can be understood as a consequence of the nanoscaled structure of the thin films used in this work. Indeed, it has been shown that the two-phase coexistence between the anatase and titanate phases is strongly dependent on particle size. When scaling the particle size below 50 nm, the increasing surface energy associated with maintaining a phase boundary inside each particle is responsible for destabilizing the intra-particle coexistence. This ultimately leads to a morphology where each nanoparticle possesses either the anatase or the titanate structure. Inside the composition range of coexistence, adding more Li^+ would simply result in an increased fraction of titanate particles at the expense of the anatase particles (53,61). The thin films studied in the current work were estimated to have particle sizes on the order of 13 nm, well below the limit for intra-particle phase coexistence.

This particle-by-particle mechanism for coexistence is compatible with the increase in lithiation entropy observed between x = 0.25 and x = 0.30. Indeed, the anatase and titanate particle ensemble will also have a configurational entropy that stems form the number of ways the titanate particles can be distributed over the total number of particles, N. Such a particle ensemble configurational entropy contribution has been proposed in nanoscaled $LiFePO_4$ as well (66). This effect can likewise be described via Equation 8, with the disorder now situated at a higher level of structural hierarchy than the Li ion-vacancy disorder inside a single intercalation compound particle. In effect, χ now represents the phase fraction. To understand the increase between x = 0.25 and x = 0.30, assume now that the former composition is still associated with the anatase structure in which incremental lithiation would cause more intercalation, and the latter corresponds to a particle-by-

particle morphology of anatase and titanate particles. The composition of x = 0.30 is situated at the start of the coexistence region, where there are many more anatase particles than titanate particles. Incremental lithiation in such a structure would result in the formation of more titanate particles. Since the phase fraction is low, Equation 8 indicates that the lithiation entropy associated with this process will be high. By contrast, at x = 0.25, the lithiation entropy is dominated by the Li ion-vacancy disorder associated with Li^+ intercalation in the anatase phase. This configurational entropy contribution is lower since the lithium content of the anatase particles is already substantial. The thermogalvanic profile, following the lithiation entropy, should then indeed increase from x = 0.25 to x = 0.30 as observed.

The decrease in the third region of the thermogalvanic profile between x = 0.35 and x = 0.45 can also be attributed to the particle ensemble's configurational entropy. Indeed, as the phase fraction of titanate grows, the configurational entropy contribution of Equation 8 will decrease, resulting in a decreasing thermogalvanic coefficient. Interestingly however, the thermogalvanic profile first increases further in the second region between x = 0.30 and x = 0.35. This finding cannot be attributed to an increase of the particle ensemble configurational entropy contribution, as the titanate phase fraction will be higher at x = 0.35 than at x = 0.30. In fact, this observation could be a result of the nonequilibrium mechanism for the anatase to titanate transition described in a previous report (61). Here, it was found that the titanate particles that formed during gradual lithiation of an anatase electrode are initially underlithiated (61). The presence of underlithiated titanate particles in the current work is supported by the time scale required for the alleviation of this deficiency via internal Li^+ redistribution. For 15 nm particles, a deficiency was reported to persist for up to 20 hours after a lithiation increment was applied (61). In the present work, the thermogalvanic coefficient of TiO_2 thin films with a similar particle size was determined 2 hours

after the preceding charging step was completed. The enduring presence of underlithiated titanate particles at the instant of the thermal response measurement is thus plausible.

It is now hypothesized that incremental lithiation of an electrode containing both anatase particles and underlithiated titanate particles proceeds along two parallel routes. First, a significant part of this Li^+ would be used to bring the underlithiated titanate particles closer to the equilibrium composition. If this further filling of the titanate particles can also be approximated as an intercalation process and the underlithiation is not too severe, the compositional parameter χ in Equation 8 is close to 1 and the associated lithiation entropy would be small. By contrast, a small amount of the incremental lithiation would also go to the creation of more titanate particles. As explained previously, this process results in a large lithiation entropy when the phase fraction of titanate is still low. Consider now that the underlithiation of the titanate phase can be expected to be less severe at higher nominal lithiation states. Upon incremental lithiation at x = 0.35, a relatively larger amount of Li^+ would then go to the high lithiation entropy process of titanate particle formation, resulting in a larger thermogalvanic coefficient for x = 0.35 than for x = 0.30. Note that this phenomenon is a nonequilibrium effect: in a true thermodynamic measurement, this increase in the thermogalvanic profile between 0.30 and 0.35 should not occur. However, the previously mentioned time scale required for full equilibration would make these experiments impractically long: using the established methodology, we estimate such a measurement would take more than 19 days.

Between x = 0.45 and x = 0.55, the thermogalvanic profile enters a fourth region wherein it forms a plateau. For large Li^+ contents, it is known that a new Li_1TiO_2 phase can form in coexistence with the titanate phase. As the thermogalvanic profile shows a plateau, this two-phase coexistence apparently results in a constant lithiation entropy in accordance with the principles

discussed above for first order phase equilibria. This indicates the Li_1TiO_2/titanate coexistence does not possess an additional level of configurational entropy as was observed for the anatase/titanate coexistence. In fact, this observation is consistent with the particle-size dependent phase diagram of anatase TiO_2: in contrast to the coexistence between anatase and titanate, the titanate and Li_1TiO_2 phases can coexist in the same particle for particle sizes up to 7 nm (53). Due to the very limited ionic conductivity of the Li_1TiO_2 phase, the morphology associated with this coexistence could for instance be a particle-shell structure (53) or a Li_1TiO_2 region covering titanate particles in an underlying film (57). Either form would not produce an additional configurational entropy contribution and is compatible with the thermogalvanic profile plateau. Finally, a fifth and last region between x = 0.55 and x = 0.65 is associated with a decreasing thermogalvanic profile. The origin of this last decrease is not yet fully clear. Potentially, it could again be associated with a particle-by-particle morphology for Li_1TiO_2 and titanate – the increasing strain of Li^+ loading may perhaps cause the particles to break apart into sizes below 7 nm which then contain either the titanate or Li_1TiO_2 phase.

To confirm our interpretation of the collected thermogalvanic profile, additional ex-situ physical characterization was performed on TiO_2 electrodes brought to a nominal composition of $Li_{0.4}TiO_2$. These films were prepared by starting a thermogalvanic profile measurement identical to that of Figure 9 but halting the process at the end of the levelling step after the 8th charge increment. Both thin film electrode samples were then removed from the cell and briefly rinsed with isopropyl alcohol. At this point in the measurement, a total charge corresponding to 0.4 Li ions per Ti atom should have been added to the films. To evaluate this composition, Elastic Recoil Detection (ERD) was performed on one of the lithiated samples as described in the SI. According to the discussion above, we expect that the composition x = 0.40 lies at the end of the coexistence region between

the anatase and titanate phases. To confirm the formation of the titanate phase and associated disappearance of the anatase phase, the other lithiated sample was investigated using XRD. For this measurement, a Bruker D8 Discover XRD system was used to attain a better signal-to-noise ratio than that of Figure 3.C. The lithiated sample was measured under an inert He atmosphere and compared to an as-deposited anatase TiO_2 reference sample. Figure 10 below shows the results of this measurement. In this Figure, only the reflections with the highest intensities in the anatase TiO2 reference spectrum (JCPDS file 02-0387) and the titanate reference spectrum (JCPDS file 77-1387) are shown with solid orange and green lines, respectively. As in Figure 3.C, the peak positions for TiN (JCPDS file 71-0299) are shown with blue dashed lines. It can be observed that the peaks at 37.9° and 55.3° corresponding to the anatase phase have virtually disappeared in the lithiated sample, and the peak at 25.3° has a much smaller intensity. Conversely, a new peak around 23.9° arises in $Li_{0.4}TiO_2$, excellently matching the most dominant reflection of the titanate phase. In conclusion, this measurement proves that anatase TiO_2 indeed converts to the titanate phase at a composition of x = 0.40 as expected from the thermogalvanic profile.
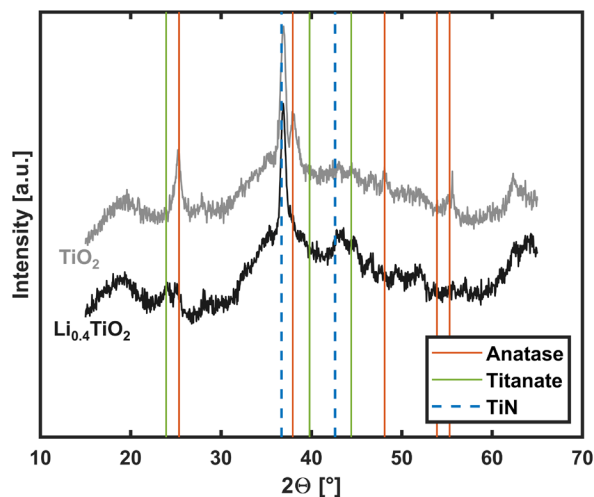
Figure 10. Figure 10. XRD spectra of an as-deposited 36 nm anatase TiO_2 thin film (in grey) and a 36 nm anatase TiO_2 thin film lithiated to a nominal composition of $Li_{0.4}TiO_2$ during a

thermogalvanic profile experiment (in black). The blue dashed lines correspond to signals from the TiN substrate while the solid orange and green lines indicate anatase and titanate peak locations, respectively.

We can now also consider the phase diagram boundaries determined here and compare them to the established values. From the thermogalvanic profile, values of x = 0.25, 0.45, and 0.65 are obtained for the anatase solubility limit and the maximum extents of anatase/titanate and titanate/Li_1TiO_2 coexistence, respectively. By contrast, approximate limits of 0.18, 0.71, and 0.91 can be expected from the phase diagram at a particle size of around 13 nm (53). There is clearly some discrepancy between these values and the present work. A first possible reason for this difference is that the particle size in the thin films examined here was not determined with a high degree of accuracy – as it was merely roughly estimated from an XRD spectrum using the Scherrer equation, a significant error may be present. Since the phase limits are strongly size-dependent, the true particle size could result in different compositional limits. Secondly, it is important to stress that the thermogalvanic profile does not represent a true equilibrium measurement, as the TiO_2 thin films were lithiated incrementally at a rate of C/4. Due to the aforementioned limited rate capability of anatase TiO_2, the equilibrium lithiation limits can likely not be reached using such a procedure. This explains why the two-phase coexistence limits determined in the present work are significantly smaller than expected. However, the anatase solubility limit appears to be greater than predicted from the phase diagram. This could be a result of the two different lithiation entropy contributions relating to underlithiated titanate particles discussed previously. It is possible that the contribution associated with a further filling of the underlithiated particles is initially of a greater magnitude than the particle ensemble configurational entropy contribution, leading to a

continued decrease of the thermogalvanic profile in the region of anatase/titanate coexistence. The true solubility limit would then lie somewhere in region 1.

4. Conclusions

This work detailed the development of a novel methodology to determine the thermogalvanic profile of Li-ion electrodes, i.e. the dependence of the thermogalvanic coefficient on the lithiation state. The methodology relied on a thermogalvanic cell with thin-film electrodes to limit thermoelectric contributions and lithium ribbons as external counter and reference electrodes to allow electrochemical control of the lithiation state.

The thermal responses collected during these experiments featured distortions such as peak drop-off and baseline drift. These effects could be fully understood as a consequence of a small amount of charge leakage between the samples under to the driving force introduced by the thermogalvanic potential difference. Due to the thin-film nature of the electrodes, these small amounts of charge leakage led to observable changes in the potential difference. When no special measures were taken, a charge difference built up over the progression of the measurement, increasing the spread on the measured coefficient and reducing reliability. To this end, a compositional levelling step was introduced. It was demonstrated that this treatment eliminates the charge buildup effect and ensures the thermogalvanic coefficient can be determined with excellent precision over the full measurement range. The spread on the thermogalvanic coefficient was shown to be no larger than the cross-sample variability of the coefficient, i.e. on the order of 0.02 mV K^{-1}.

In addition to this excellent precision, the second major strength of the developed method is its capacity to collect thermogalvanic profiles with a high lithiation state resolution. Indeed, small lithiation increments of $\Delta x = 0.05$ were used to validate the methodology by determining the thermogalvanic profile of thin-film anatase TiO$_2$. The accuracy of the developed methodology was

proven by demonstrating that the collected profile could be fully explained by established knowledge of the phase behavior in this material. It is significant that the aforementioned high resolution allowed the identification of nanoscaling effects in the thermogalvanic profile. More specifically, the evolution from intra-particle coexistence to a particle-by-particle morphology for anatase and titanate at small particle sizes led to a sloping profile in the coexistence region rather than the flat profile that would be expected for a bulk material. In effect, this work confirms that thermogalvanic or entropy profiles can also serve as a relatively inexpensive (though indirect) tool to probe the effects of nanoscaling on the phase behavior of an electrode material: thermogalvanic methods rely on an electrochemical measurement instead of more costly infrastructure required for scattering or spectroscopic techniques (42). The fact that such nanoscaling effects, which manifest as variations in the local value of the thermogalvanic coefficient, can accurately be detected with the methodology developed in the present work once more highlights the value of our technique.

In the future, our novel methodology can be applied to study the thermogalvanic profiles of a wider catalogue of active electrode materials. Knowledge of these thermogalvanic properties can ultimately result in harvesting devices with high temperature coefficients, for instance by pairing materials with dissimilar coefficients in TREC cells. In any final device, it will also be important to consider the kinetic limitations of the selected electrode materials since internal losses will determine what fraction of the thermogalvanically harvested potential difference can ultimately be used to power an IoT node. As such, this work opens the door for more research on thermogalvanic harvesting based on Li-ion electrodes – a strategy that could eventually enable more performant, efficient, and scalable IoT solutions.

ASSOCIATED CONTENT

Supporting Information

Supporting Information Available: Steady-state temperature distribution in the thermogalvanic cell, additional comments on compositional levelling, additional comments on the estimation of potential difference changes due to charge leakage, ERD measurement of lithiated TiO_2 thin film electrode (PDF). This material is available free of charge via the Internet at https://pubs.acs.org/.

AUTHOR INFORMATION

Corresponding Author

*Philippe M. Vereecken – KU Leuven Centre for Membrane Separations, Adsorption, Catalysis, and Spectroscopy for Sustainable Solutions, Celestijnenlaan 200f - box 2454, Leuven, 3001, Belgium; imec, Kapeldreef 75, Leuven, 3001, Belgium; orcid.org/0000-0003-4115-0075; Email: philippe.vereecken@imec.be

Author

Liese B. Hubrechtsen – KU Leuven Centre for Membrane Separations, Adsorption, Catalysis, and Spectroscopy for Sustainable Solutions, Celestijnenlaan 200f - box 2454, Leuven, 3001, Belgium; imec, Kapeldreef 75, Leuven, 3001, Belgium; orcid.org/0000-0003-4546-2316; Email: liese.hubrechtsen@imec.be

Notes

The authors declare no competing financial interest.

ACKNOWLEDGMENTS

REFERENCES

1.   Dey N, Mahelle P, Mohd Shafi P, Kimabahune V, Hassanien AE. Internet of Things, Smart Computing and Technology: A Roadmap Ahead. Vol. 266, Studies in Systems, Decision and Control. Warsaw: Springer; 2020.

2.   Doherty L, Warneke BA, Boser BE, Pister KSJ. Energy and Performance Considerations for Smart Dust. Int J Parallel Distrib Syst Networks. 2001;4:121–133.

3.   Snyder GJ, Toberer ES. Complex Thermoelectric Materials. Nat Mater. 2008;7:105–114.

4.   Freer R, Powell A V. Realising the Potential of Thermoelectric Technology: A Roadmap. J Mater Chem C. 2020;8:441–463.

5.   Hudak NS, Amatucci GG. Energy Harvesting and Storage with Lithium-Ion Thermogalvanic Cells. J Electrochem Soc. 2011;158:A572–A579.

6.   Dupont MF, MacFarlane DR, Pringle JM. Thermo-Electrochemical Cells for Waste Heat Harvesting-Progress and Perspectives. Chem Commun. 2017;53:6288–6302.

7.   Gunawan A, Lin CH, Buttry DA, Mujica V, Taylor RA, Prasher RS, Phelan PE. Liquid thermoelectrics: Review of Recent and Limited New Data of Thermogalvanic Cell Experiments. Nanoscale Microscale Thermophys Eng. 2013;17:304–323.

8.   Duan J, Feng G, Yu B, Li J, Chen M, Yang P, Feng J, Liu K, Zhou J. Aqueous Thermogalvanic Cells with a High Seebeck Coefficient for Low-Grade Heat Harvest. Nat Commun. 2018;9:1–8.

9.   Buckingham MA, Zhang S, Liu Y, Chen J, Marken F, Aldous L. Thermogalvanic and Thermocapacitive Behavior of Superabsorbent Hydrogels for Combined Low-Temperature Thermal Energy Conversion and Harvesting. ACS Appl Energy Mater. 2021;4:11204–11214.

10.   Yu B, Duan J, Cong H, Xie W, Liu R, Zhuang X, Wang H, Qi B, Xu M, Wang ZL et al. Thermosensitive Crystallization-Boosted Liquid Thermocells for Low-Grade Heat Harvesting. Science. 2020;370:342–346.

11.   Yang P, Liu K, Chen Q, Mo X, Zhou Y, Li S, Feng G, Zhou J. Wearable Thermocells Based on Gel Electrolytes for the Utilization of Body Heat. Angew Chemie - Int Ed. 2016;55:12050–12053.

12.   Ding T, Zhou Y, Wang XQ, Zhang C, Li T, Cheng Y, Lu W, He J, Ho GW. All-Soft and Stretchable Thermogalvanic Gel Fabric for Antideformity Body Heat Harvesting Wearable. Adv Energy Mater. 2021;11:2102219.

13.   Agar JN. Thermogalvanic Cells. In: Delahay P, editor. Advances in Electrochemistry and Electrochemical Engineering. New York: Wiley; 1963. 31–121.

14. Agar JN. The rate of Attainment of Soret Equilibrium. Trans Faraday Soc. 1960;56:776–787.

15. Eastman ED. Theory of the Soret Effect. J Am Chem Soc. 1928;50:283–291.

16. Han C, Qian X, Li Q, Deng B, Zhu Y, Han Z, Zhang W, Wang W, Feng S, Chen G et al. Giant Thermopower of Ionic Gelatin Near Room Temperature. Science. 2020;368:1091–1098.

17. Quickenden TI. A Review of Power Generation in Aqueous Thermogalvanic Cells. J Electrochem Soc. 1995;142:3985–3994.

18. Buckingham MA, Aldous L. Thermogalvanic Cells: A Side-By-Side Comparison of Measurement Methods. J Electroanal Chem. 2020;872:114280.

19. Zhang H, Zhang F, Yu J, Zhou M, Luo W, Lee YM, Si M, Wang Q. Redox Targeting-Based Thermally Regenerative Electrochemical Cycle Flow Cell for Enhanced Low-Grade Heat Harnessing. Adv Mater. 2021;33:2006234.

20. Chum HL, Osteryoung RA. Review of Thermally Regenerative Electrochemical Systems. Golden, CO; 1981.

21. Rahimi M, Straub AP, Zhang F, Zhu X, Elimelech M, Gorski CA, Logan BE. Emerging Electrochemical and Membrane-Based Systems to Convert Low-Grade Heat to Electricity. Energy Environ Sci. 2018;11:276–285.

22. Jiang J, Tian H, He X, Zeng Q, Niu Y, Zhou T, Yang Y, Wang C. A CoHCF System with Enhanced Energy Conversion Efficiency for Low-Grade Heat Harvesting. J Mater Chem A. 2019;7:23862–23867.

23.   Liu Y, Gao C, Sim S, Kim M, Lee SW. Lithium Manganese Oxide in an Aqueous Electrochemical System for Low-Grade Thermal Energy Harvesting. Chem Mater. 2019;31:4379–4384.

24.   Gao C, Lee SW, Yang Y. Thermally Regenerative Electrochemical Cycle for Low-Grade Heat Harvesting. ACS Energy Lett. 2017;2:2326–2334.

25.   Lee SW, Yang Y, Lee HW, Ghasemi H, Kraemer D, Chen G, Cui Y. An Electrochemical System for Efficiently Harvesting Low-Grade Heat Energy. Nat Commun. 2014;5:1–6.

26.   Yang Y, Lee SW, Ghasemi H, Loomis J, Li X, Kraemer D, Zheng G, Cui Y, Chen G. Charging-Free Electrochemical System for Harvesting Low-Grade Thermal Energy. Proc Natl Acad Sci U S A. 2014;111:17011–17016.

27.   Yang Y, Loomis J, Ghasemi H, Lee SW, Wang YJ, Cui Y, Chen G. Membrane-Free Battery for Harvesting Low-Grade Thermal Energy. Nano Lett. 2014;14:6578–6583.

28.   Linford PA, Xu L, Huang B, Shao-Horn Y, Thompson C V. Multi-Cell Thermogalvanic Systems for Harvesting Energy from Cyclic Temperature Changes. J Power Sources. 2018;399:429–435.

29.   Gao C, Yin Y, Zheng L, Liu Y, Sim S, He Y, Zhu C, Liu Z, Lee H, Yuan Q et al. Engineering the Electrochemical Temperature Coefficient for Efficient Low-Grade Heat Harvesting. Adv Funct Mater. 2018;28:1–7.

30.   Zubi G, Dufo-López R, Carvalho M, Pasaoglu G. The Lithium-Ion Battery: State of the Art and Future Perspectives. Renew Sustain Energy Rev. 2018;89:292–308.

31.   Hayner CM, Zhao X, Kung HH. Materials for Rechargeable Lithium-Ion Batteries. Annu Rev Chem Biomol Eng. 2012;3:445–471.

32.   Sepúlveda A, Speulmanns J, Vereecken PM. Bending Impact on the Performance of a Flexible Li4Ti5O12-Based All-Solid-State Thin-Film Battery. Sci Technol Adv Mater. 2018;19:454–464.

33.   Luntz AC, Voss J, Reuter K. Interfacial Challenges in Solid-State Li Ion Batteries. J Phys Chem Lett. 2015;6:4599–4604.

34.   Schichtel P, Geiß M, Leichtweiß T, Sann J, Weber DA, Janek J. On the Impedance and Phase Transition of Thin Film All-Solid-State Batteries Based on the Li4Ti5O12 System. J Power Sources. 2017;360:593–604.

35.   Moitzheim S, Put B, Vereecken PM. Advances in 3D Thin-Film Li-Ion Batteries. Adv Mater Interfaces. 2019;6:1–17.

36.   Dudney NJ. Evolution of the Lithium Morphology from Cycling of Thin Film Solid State Batteries. J Electroceramics. 2017;38:222–229.

37.   Rambabu A, Krupanidhi SB, Barpanda P. An Overview of Nanostructured Li-based Thin Film Micro-Batteries. Proc Indian Natl Sci Acad. 2018;85:121–142.

38.   Put B, Vereecken PM, Labyedh N, Sepulveda A, Huyghebaert C, Radu IP, Stesmans A. High Cycling Stability and Extreme Rate Performance in Nanoscaled LiMn2O4 Thin Films. ACS Appl Mater Interfaces. 2015;7:22413–22420.

39.   Put B, Vereecken PM, Meersschaut J, Sepúlveda A, Stesmans A. Electrical Characterization of Ultrathin RF-Sputtered LiPON Layers for Nanoscale Batteries. ACS Appl Mater Interfaces. 2016;8:7060–7069.

40.   Kuzminskii Y V., Zasukha VA, Kuzminskaya GY. Thermoelectric Effects in Electrochemical Systems. Nonconventional Thermogalvanic Cells. J Power Sources. 1994;52:231–242.

41.   Viswanathan V V., Choi D, Wang D, Xu W, Towne S, Williford RE, Zhang J, Liu J, Yang Z. Effect of Entropy Change of Lithium Intercalation in Cathodes and Anodes on Li-Ion Battery Thermal Management. J Power Sources. 2010;195:3720–3729.

42.   Yazami R. Thermodynamics of Electrode Materials for Lithium-Ion Batteries. Lithium Ion Rechargeable Batteries: Materials, Technology, and New Applications. 2010. p. 67–102.

43.   Reynier Y, Graetz J, Swan-Wood T, Rez P, Yazami R, Fultz B. Entropy of Li Intercalation in LixCoO2. Phys Rev B - Condens Matter Mater Phys. 2004;70:1–7.

44.   Zhang XF, Zhao Y, Patel Y, Zhang T, Liu WM, Chen M, Offer GJ, Yan Y. Potentiometric Measurement of Entropy Change for Lithium Batteries. Phys Chem Chem Phys. 2017;19:9833–9842.

45.   Osswald PJ, Del Rosario M, Garche J, Jossen A, Hoster HE. Fast and Accurate Measurement of Entropy Profiles of Commercial Lithium-Ion Cells. Electrochim Acta. 2015;177:270–276.

46.   Doh CH, Ha YC, Eom SW. Entropy Measurement of a Large Format Lithium Ion Battery and its Application to Calculate Heat Generation. Electrochim Acta. 2019;309:382–391.

47.   Allart D, Montaru M, Gualous H. Model of Lithium Intercalation into Graphite by Potentiometric Analysis with Equilibrium and Entropy Change Curves of Graphite Electrode. J Electrochem Soc. 2018;165:A380–A387.

48.   Al Hallaj S, Venkatachalapathy R, Prakash J, Selman JR. Entropy Changes Due to Structural Transformation in the Graphite Anode and Phase Change of the LiCoO2 Cathode. J Electrochem Soc. 2000;147:2432–2436.

49.   Jung SK, Hwang I, Chang D, Park KY, Kim SJ, Seong WM, Eum D, Park J, Kim B, Kim J et al. Nanoscale Phenomena in Lithium-Ion Batteries. Chem Rev. 2020;120:6684–6737.

50.   Jamnik J, Maier J. Nanocrystallinity Effects in Lithium Battery Materials: Aspects of Nano-Ionics. Part IV. Phys Chem Chem Phys. 2003;5:5215–5220.

51.   Li D, Zhou H. Two-Phase Transition of Li-Intercalation Compounds in Li-Ion Batteries. Mater Today. 2014;17:451–463.

52.   Borghols WJH, Wagemaker M, Lafont U, Kelder EM, Mulder FM. Size Effects in the Li4+xTi5O12 Spinel. J Am Chem Soc. 2009;131:17786–17792.

53.   Wagemaker M, Borghols WJH, Mulder FM. Large Impact of Particle Size on Insertion Reactions. A Case for Anatase LixTiO2. J Am Chem Soc. 2007;129:4323–4327.

54.   Okubo M, Mizuno Y, Yamada H, Kim J, Hosono E, Zhou H, Kudo T, Honma I. Fast Li-Ion Insertion into Nanosized LiMn2O4 without Domain Boundaries. ACS Nano. 2010;4:741–752.

55.   Moitzheim S. Fabrication and Characterization of 3D Thin-Film Batteries Titanium Dioxide As Candidate for High Rate and High Capacity Microstorage Devices [dissertation]. Leuven: KU Leuven; 2018.
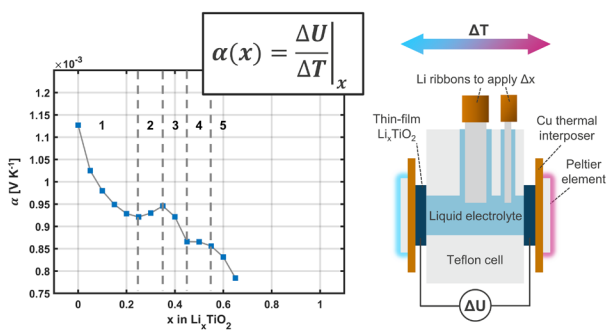
56.   Liu Y, Yang Y. Recent Progress of TiO2-Based Anodes for Li Ion Batteries. J Nanomater. 2016;2016.

57.   Moitzheim S, De Gendt S, Vereecken PM. Investigation of the Li-Ion Insertion Mechanism for Amorphous and Anatase TiO2 Thin-Films. J Electrochem Soc. 2019;166:A1–A9.

58.   Ye J, Baumgaertel AC, Wang YM, Biener J, Biener MM. Structural Optimization of 3D Porous Electrodes for High-Rate Performance Lithium Ion Batteries. ACS Nano. 2015;9:2194–2202.

59.   Shen Y, Chen JS, Zhu J, Yan Q, Hu X. Growth of Two-Dimensional Ultrathin Anatase TiO2 Nanoplatelets on Graphene for High-Performance Lithium-Ion Battery. J Nanoparticle Res. 2013;15:1913.

60.   Cava RJ, Murphy DW, Zahurak S, Santoro A, Roth RS. The Crystal Structures of the Lithium-Inserted Metal Oxides Li0.5TiO2 Anatase, LiTi2O4 Spinel, and Li2Ti2O4. J Solid State Chem. 1984;53:64–75.

61.   Shen K, Chen H, Klaver F, Mulder FM, Wagemaker M. Impact of Particle Size on the Non-Equilibrium Phase Transition of Lithium-Inserted Anatase TiO2. Chem Mater. 2014;26:1608–1615.

62.   Morgan BJ, Watson GW. Role of Lithium Ordering in the LixTiO2 Anatase → Titanate Phase Transition. J Phys Chem Lett. 2011;2:1657–1661.

63.   Sudant G, Baudrin E, Larcher D, Tarascon JM. Electrochemical Lithium Reactivity with Nanotextured Anatase-Type TiO2. J Mater Chem. 2005;15:1263–1269.

64. Pomjaksilp S. pyMeCom. https://github.com/spomjaksilp/pyMeCom.git (accessed 2022-03-22).

65. Ottermann CR, Bange K. Correlation Between the Density of TiO2 Films and Their Properties. Thin Solid Films. 1996;286:32–34.

66. Kai K, Kobayashi Y, Miyashiro H, Oyama G, Nishimura SI, Okubo M, Yamada A. Particle-Size Effects on the Entropy Behavior of a LixFePO4 Electrode. ChemPhysChem. 2014;15:2156–2161.

TABLE OF CONTENTS GRAPHIC

For Table of Contents Only